AAS 23-142

CLUSTERING APPROACH TO IDENTIFYING LOW LUNAR FROZEN ORBITS IN A HIGH-FIDELITY MODEL

Giuliana E. Miceli,[*] Natasha Bosanac,[†] Michael A. Mesarch,[‡] David C. Folta,[§] and Rebecca L. Mesarch [¶]

Low lunar frozen orbits are of continued interest in the astrodynamics community for trajectory design and space domain awareness. This paper presents a data-driven approach to analyzing a wide variety of numerically-generated lunar trajectories in a 100×100 lunar gravity model with the point mass gravity of the Earth and Sun. First, clustering is used to extract a summary of these trajectories: within each cluster, trajectories possess a geometrically similar evolution of perilune but varying drift and lifetimes. Within some clusters, trajectories with a bounded perilune evolution are also identified to produce candidates for lunar frozen orbits of distinct geometries.

INTRODUCTION

Since the early 1960s, astrodynamicists have studied frozen orbits: trajectories that exhibit small variations in the orbital elements relative to a selected celestial body over long time intervals.[1] Near the Moon, frozen orbits–or even quasi-frozen orbits with a bounded variation in the orbital elements–have been of significant interest for designing mission orbits that require little maintenance over long time intervals. These trajectories can support scientific missions, placement of critical infrastructure, and extended imaging of the lunar surface. In fact, previous missions have already leveraged frozen and quasi-frozen lunar orbits identified in high-fidelity gravity models to limit station-keeping maneuver requirements, including Lunar Prospector (1997-1999) and the Lunar Reconnaissance Orbiter (2009 - present).[2,3] Furthermore, frozen and quasi-frozen lunar orbits may be useful for space domain awareness when locating objects or debris that may remain in a lunar orbit for long time intervals.

A common existing approach to identifying and characterizing lunar frozen orbits is to use analytical approximations in truncated dynamical models. As an example, Ely examined the evolution of the orbital elements in a point mass lunar gravity model with a third-body perturbation from the Earth to identify elliptical and inclined lunar frozen orbits.[4] Folta and Quinn use a similar approach to identify lunar frozen orbits that are then numerically simulated in a higher fidelity ephemeris

*Graduate Research Assistant, Colorado Center for Astrodynamics Research, Smead Department of Aerospace Engineering Sciences, University of Colorado Boulder, Boulder, CO, 80303.

†Assistant Professor, Colorado Center for Astrodynamics Research, Smead Department of Aerospace Engineering Sciences, University of Colorado Boulder, Boulder, CO, 80303.

‡Aerospace Engineer, Navigation and Mission Design Branch, NASA Goddard Space Flight Center, Greenbelt MD, 20771.

§Senior Fellow, Navigation and Mission Design Branch, NASA Goddard Space Flight Center, Greenbelt MD, 20771.

¶Aerospace Engineer, Navigation and Mission Design Branch, NASA Goddard Space Flight Center, Greenbelt MD, 20771.

model and also leveraged for maneuver design.[5] Additionally, Elipe and Lara used corrections and continuation algorithms to compute frozen orbits in a lunar gravity model that captures the first 7 zonal harmonic terms, identifying three distinct families of lunar frozen orbits across various eccentricities and inclinations.[6] Lara, Ferrer, and De Saedeleer then used an averaged Hamiltonian formulation of a lunar gravity model with the first 50 zonal harmonics and the point mass gravity of the Earth to examine the long-term behavior of low lunar polar orbits.[7] A wide variety of researchers have used similar approaches to identify frozen orbits in low-order spherical harmonic gravity models of the Moon that are augmented by the gravitational influence of the Earth.[8–10]

Alternatively, low lunar frozen orbits may be identified numerically in a high-fidelity dynamical model. As an example, Russell and Lara identified families of multi-revolution periodic orbits near the Moon via numerical integration and differential corrections in an Earth-Moon restricted three-body model that is augmented with a 50×50 lunar gravity model.[11] Further generalizing the numerical identification of low lunar frozen orbits, a large number of trajectories can be numerically integrated over a specified time interval from a wide array of initial conditions and then examined. However, with this approach, a significant challenge emerges: extracting long-term bounded motions that may correspond to frozen or quasi-frozen orbits from a diverse array of trajectories.

Reframing trajectory analysis as a data analysis problem reveals a challenge shared across many technical disciplines: extracting meaningful insight from large datasets without overburdening a human analyst or requiring a priori knowledge. Clustering techniques have proven useful in addressing these challenges by automatically grouping similar data into a cluster and separating dissimilar data into distinct clusters.[12] The resulting clusters supply a digestible, data-driven summary of the dataset that may simplify analysis and drive knowledge discovery. This approach has proven valuable in a variety of disciplines: in medicine, clustering has been used to detect clinically meaningful shape clusters in medical image data, and in astronomy clustering has been used to identify distinct types of galaxies.[13,14] In astrodynamics, clustering has been used to detect bounded motions near distant retrograde orbits, group periodic orbits that are independently computed, extract motion primitive sets that summarize families of trajectories, and summarize a wide variety of trajectories in the Sun-Earth circular restricted three-body problem at a single energy level.[15–20]

This paper presents a clustering-based approach to summarizing a wide variety of trajectories that are numerically generated in a high-fidelity lunar gravity model. This summary is used to extract insight into the solution space and locate motions with a bounded evolution of perilune that may supply candidates for low lunar frozen and quasi-frozen orbits. First, we define initial conditions as perilunes with distinct combinations of orbital elements. To support a proof of concept, these perilunes possess a fixed semi-major axis of 1838 km and an initial epoch on January 1, 2025. Trajectories are generated for up to 180 days from these initial conditions in a 100×100 lunar gravity model with the point mass gravity of the Earth and Sun. This model fidelity is selected to balance prediction accuracy against computational time. Consistent with previous analyses of frozen orbits, we then characterize each trajectory by the time evolution of the eccentricity and argument of periapsis at each perilune in a Moon-fixed frame defined using principal axes. The evolution of perilune over 180 days is then summarized to produce a finite-dimensional feature vector that encodes its size and shape. Next, Hierarchical Density-Based Spatial Clustering of Applications with Noise (HDBSCAN) is used to cluster these feature vectors in a two-step process.[21] Each cluster corresponds to trajectories with a geometrically similar evolution of perilune. The result is a clustering-based summary of the geometries exhibited by trajectories near the Moon that is also used to identify candidates for low lunar frozen or quasi-frozen orbits.

GENERATING LUNAR TRAJECTORIES

In this paper, two reference frames are used to describe the state of a spacecraft relative to the center of the Moon. First, a Moon-centered inertial frame is defined using the center of the Moon as the origin and the axes $\hat{X}, \hat{Y}, \hat{Z}$ of the International Celestial Reference Frame (ICRF).[22] In addition, a Moon-fixed frame is defined using lunar principal axes.[23] These principal axes are accessed using the moon_080317 kernel file that is provided by NASA's Navigation and Ancillary Information Facility (NAIF) and compatible with the DE421 lunar and planetary ephemerides.[24,25]

Trajectories are generated in a high-fidelity lunar gravity model augmented by the point mass gravity of the Earth and Sun. In the Moon-centered inertial frame, the state vector for the spacecraft relative to the Moon is defined as $\bar{X} = [X, Y, Z, \dot{X}, \dot{Y}, \dot{Z}]^T = [\bar{R}_{L,sc}, \bar{V}_{L,sc}]^T$. The equations of motion governing the spacecraft, assumed to possess a comparatively negligible mass, are then written as

$$\ddot{\bar{R}}_{L,sc} = -GM_L \left(\frac{\bar{R}_{L,sc}}{R^3_{L,sc}} \right) + G \sum_{i=E,S} M_i \left(\frac{\bar{R}_{sc,i}}{R^3_{sc,i}} - \frac{\bar{R}_{L,i}}{R^3_{L,i}} \right) + \bar{a}_L \tag{1}$$

where the subscripts L, E, S, and sc indicate the Moon, Earth, Sun, and spacecraft, M_i is the mass of body i, G is the universal gravitational constant, $\dot{(.)}$ indicates a time derivative with respect to an observer in the inertial frame, $\bar{R}_{i,j}$ indicates the position vector measured from body i to body j, and $\bar{a}_L$ captures the acceleration due to higher-order lunar gravity terms. The DE421 lunar and planetary ephemerides, maintained by NASA's NAIF, are used to locate each celestial body at each epoch during numerical integration.[26] Additional perturbing accelerations are not included in this proof of concept.

The lunar gravity field is represented by a 100×100 degree and order spherical harmonics model. In the Moon-fixed frame, defined using principal axes, the potential function for the deviation of the gravity field from a point mass equals

$$U_L = \frac{GM_L}{r} \left[\sum_{l=2}^{100} \sum_{m=0}^{l} \left(\frac{R_L}{r} \right)^l P_{l,m} \left(\sin(\phi) \right) \left(C_{l,m} \cos(m\lambda) + S_{l,m} \sin(m\lambda) \right) \right] \tag{2}$$

where R_L is the reference radius of the Moon, $P_{l,m}$ is the associated Legendre polynomial for degree l and order m, ϕ and λ are the selenocentric latitude and longitude, and $C_{l,m}$ and $S_{l,m}$ are the coefficients of the spherical harmonic expansion.[27] In this work, the coefficients of expansion and model parameters are accessed using the 900×900 gravity model (GRGM900C) which is compatible with the DE421 ephemerides.[28] Then, a frame transformation is applied to the vector derivative of the potential function to calculate the acceleration $\bar{a}_L$ in the Moon-inertial frame. Although higher degree and order gravity coefficients are available in this and other models, they are not included in this paper due to their significant influence on the computational time. Furthermore, the Lunar Prospector mission's successful use of a quasi-frozen lunar orbit that was identified in a 100×100 degree and order gravity model indicates that this level of truncation may supply sufficient prediction accuracy.[29]

CLUSTERING

Clustering is a method for grouping members of a dataset based on a specified set of features without requiring a human-in-the-loop. Clustering algorithms are often categorized as hierarchical-based, partitioning-based, density-based, grid-based, and/or model-based.[30] Furthermore, hard clustering uniquely assigns each member of a dataset to a single cluster, whereas fuzzy clustering assigns probabilities of cluster membership.

This paper uses the Hierarchical Density-Based Spatial Clustering of Applications with Noise (HDBSCAN) algorithm developed by Campello, Moulavi, and Sander to group trajectories.[31] HDBSCAN is a hard clustering algorithm that discovers clusters of arbitrary shape and density that are separated by an unknown or nonconstant distance. Furthermore, HDBSCAN does not require a priori knowledge of the number of clusters and labels data in insufficiently sampled regions as noise. Because of these characteristics, HDBSCAN has successfully been used in a variety of fields from medicine to computer vision.[32,33] This clustering algorithm has also previously been demonstrated by Bosanac as well as Bonasera and Bosanac to successfully cluster spacecraft trajectories by their geometry in a chaotic dynamical model.[19,20]

HDBSCAN uses a hierarchical and density-based approach to group the N members of a dataset, each described by m-dimensional feature vectors that capture user-specified characteristics of interest. This process is summarized here; for a more detailed explanation, see Campello, Moulavi, and Sander 2013.[31] First, the core distance d_{core}, is computed for each member. For the i-th member, this quantity is defined as the distance of the feature vector $\bar{v}_i$ from its $(n_{sample} - 1)$-th nearest neighbor, assessed using a specified distance measure. The core distance is used to calculate the mutual reachability distance (MRD) between each pair of feature vectors $\bar{v}_i$ and $\bar{v}_j$ as $d_{mreach} = \max(d_{core}(\bar{v}_i), d_{core}(\bar{v}_j), d(\bar{v}_i, \bar{v}_j))$, where $d(\bar{v}_i, \bar{v}_j)$ is the distance between $\bar{v}_i$ and $\bar{v}_j$. Using this information, a mutual reachability graph is constructed with N nodes defined as the feature vectors and the edges between each pair of nodes weighted by the MRD of the associated feature vectors. This graph is summarized using a minimum spanning tree (MST) that is augmented by adding self-loops to each node that are weighted by the core distance of its feature vector. HDBSCAN then constructs a dendrogram from this augmented MST to produce a clustering hierarchy. Clusters are identified from this hierarchy as groups of members that are sufficiently stable as a function of density and possess a size that is above a minimum value, denoted n_{size}. In a modification to the HDBSCAN algorithm, presented by Malzer and Baum, clusters with a distance below a threshold ϵ are merged.[34] Finally, if the local neighborhood of a member of the dataset does not encompass at least $(n_{sample} - 1)$ neighbors, that member is labeled as a noise point. The output of this process is a set of labels assigning each of the N members of the dataset to either a cluster or a noise group. In this paper, HDBSCAN is accessed via the *hdbscan* clustering library in Python.[35]

The Density-Based Clustering Validation (DBCV) index introduced by Moulavi et al. is used to assess the quality of a clustering result generated by HDBSCAN.[36] The DBCV index measures the ratio of the inter-cluster separation to the intra-cluster density with values between -1 and 1; a high value of the DBCV index indicates a better clustering result with clusters that are more tightly packed and well-separated. Mathematically, the DBCV index is defined for a dataset that has been grouped into n_{clust} clusters as

$$DBCV = \sum_{i=1}^{n_{clust}} \frac{C_i}{T} V_C(C_i) \tag{3}$$

where T is the total number of points and $V_C(C_i)$ is the validity index of cluster C_i, defined as

$$V_C(C_i) = \frac{\min_{1\leq j\leq l, j\neq i}(DSPC(C_i, C_j)) - DSC(C_i)}{\max(\min_{1\leq j\leq l, j\neq i}(DSPC(C_i, C_j)), DSC(C_i))} \tag{4}$$

where $DSPC$ is the density separation of a pair of clusters, defined as the minimum reachability distance between the internal nodes of the MST of clusters C_i and C_j; and DSC is the density sparseness of a cluster defined as the maximum edge weight of the internal edges in MST of the cluster C_i. This validity index compares the internal density compactness of a cluster and the density separation between two clusters with a positive value of $V_C(C_i)$ indicating a better cluster that is compact and well separated from other clusters.

TECHNICAL APPROACH

This paper presents a clustering-based framework for summarizing lunar trajectories and extracting bounded orbits that may supply candidates for frozen and quasi-frozen orbits. This framework consists of the following steps:

1. Numerically generating a set of trajectories in a selected dynamical model
2. Describing each trajectory using a finite-dimensional feature vector
3. Clustering the dataset to produce groups of spatiotemporally similar trajectories
4. Summarizing each cluster using a representative member
5. Merging clusters with geometrically similar representatives

Step 1: Generating a set of lunar trajectories

To generate a set of lunar trajectories, a wide range of initial conditions are defined using Keplerian orbital elements at a fixed epoch and semi-major axis. Although epoch and semi-major axis are both variables that impact the characteristics of the associated trajectories, they are constrained in this paper to reduce the size of the dataset and support a proof of concept. The ranges and step sizes of each orbital element are listed in Table 1. All the possible combinations of these orbital elements result in 58,608 initial conditions that lie above the lunar radius, assumed to equal 1738 km in this paper. Each initial condition is propagated for up to 180 days or until reaching the lunar radius. This numerical propagation is performed in the high-fidelity dynamical model presented earlier. To limit data storage requirements, only the perilune states are recorded along each trajectory.

Table 1. Ranges of orbital elements used to define initial conditions.

Orbital Element	Value/s	Step
Epoch, T_0	January 1, 2025 00:00.000 UTC	-
Semi-major axis, a	1838 km	-
Eccentricity, e	$[10^{-4}, 0.1]$	0.005
Inclination, i (in Moon-fixed frame)	$[0.001°, 179.999°]$	5°
Right ascension of the ascending node (RAAN), Ω (in Moon-fixed frame)	$[0°, 360°]$	30°
Argument of periapsis (AOP), ω (in Moon-fixed frame)	$[0°, 360°]$	30°

Step 2: Describing each trajectory via a feature vector

Consistent with traditional analyses of frozen orbits, each lunar trajectory is represented in this paper by the evolution of perilune over time. Researchers have commonly searched for frozen orbits as trajectories with a bounded variation in the eccentricity and argument of periapsis;[5,37,38] some researchers also use alternative orbital element sets.[6,39] In this paper, each perilune is partially described using the variables $p = e\cos(\omega)$ and $q = e\sin(\omega)$ because they possess equivalent value ranges but visualized in an $e - \omega$ polar plot for clarity. To demonstrate the value of this

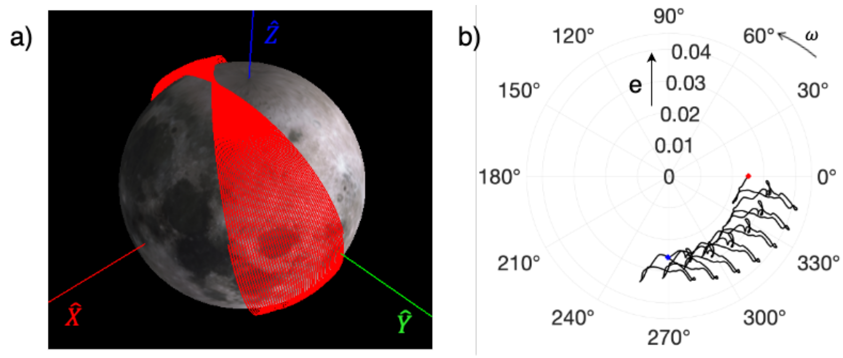

Figure 1. a) A 4-day segment of a lunar trajectory in the Moon-fixed frame generated from a perilune with $e = 0.025,\ i = 85°,\ \omega = 0°,\ \Omega = 210°$. b) Associated evolution of perilune over 180 days in an $e - \omega$ polar plot; red and blue markers indicate the initial and final perilunes.

low-dimensional representation, Figure 1a) displays a 4-day segment of a lunar trajectory in the Moon-fixed frame that is generated from an initial perilune with the following orbital elements: $e = 0.025,\ i = 85°,\ \omega = 0°,\ \Omega = 210°$. The associated evolution of each perilune over 180 days in the Moon-fixed frame is then plotted in black in Figure 1b) on an $e - \omega$ polar plot with the first and last perilune located by red and blue markers, respectively. Using this figure as an example, trajectories that are generated for at least 27.3 days tend to possess an evolution of perilune that exhibits multiple revolutions in the pq-plane and $e - \omega$ polar plot, with each revolution occurring over one lunar rotational period, i.e., 27.3 days.[40] This geometric property is exploited in later steps of the clustering framework.

The evolution of the perilunes along each trajectory is summarized using a feature vector that can be input to a clustering algorithm. In general, the feature vector $\bar{v}_i$ is a finite-dimensional representation of the characteristics of interest for the i-th member of a dataset $\bar{V}$. In this paper, this feature vector is constructed to capture the spatiotemporal evolution of these perilunes. First, a fixed number of m perilunes are evenly sampled from the perilunes along each trajectory. Using a fixed number of samples for all trajectories enables the definition of a feature vector with a fixed length along the entire dataset and, therefore, the use of fast distance measures during clustering. In this paper, $m = 90$ is selected empirically: for the trajectories in our dataset, 15 perilunes along each lunar rotational period can sufficiently describe the perilune evolution shape. Then, $\bar{s}_{i,k}$ is defined as a unit vector directed from the k-th perilune to the $k+1$-th perilune along the i-th trajectory in the $p - q$ plane. Mathematically, this unit vector is defined as

$$\bar{s}_{i,k} = \frac{[p_{i,k+1} - p_{i,k}, q_{i,k+1} - q_{i,k}]}{||[p_{i,k+1} - p_{i,k}, q_{i,k+1} - q_{i,k}]||} \tag{5}$$

At the k-th perilune along the i-th trajectory generated over an integration time of t_{max}, a normalized elapsed time is also defined as

$$\tilde{t}_{i,k} = \frac{t_{i,k}}{t_{max}} \tag{6}$$

Using these two quantities, the feature vector for the i-th trajectory is defined as

$$\bar{v}_i = [\bar{s}_{i,1}, \bar{s}_{i,2}, ..., \bar{s}_{i,m-1}, \tilde{t}_{i,1}, \tilde{t}_{i,2}, ...\tilde{t}_{i,m}] \tag{7}$$

producing a $(3m-2)$-dimensional description. This feature vector approximates the shape of the discrete path formed by the perilunes along a trajectory in the pq-plane as well as its phasing.

Step 3: Clustering the trajectories by geometry and phasing

To cluster the feature vectors generated in Step 2 using HDBSCAN, multiple governing parameters must be selected. First, the Euclidean distance is used to assess the difference between feature vectors $\bar{v}_i$ and $\bar{v}_j$, labeled as $d_e(\bar{v}_i, \bar{v}_j)$. Although the Euclidean distance only compares two time-ordered sequences as opposed to two geometric paths, this distance metric is used because it enables fast and computationally-tractable clustering for a large dataset. Then, a grid search is used along with cluster validation techniques to select suitable values of n_{sample} and n_{size}. This grid search is performed by generating clustering results for various combinations of $n_{sample} = [2, 26]$ with a step size of 4 and $n_{size} = [30, 100]$ with a step size of 10. After clustering the generated set of trajectories using HDBSCAN for all possible combinations of these parameters, n_{sample} and n_{size} are selected to balance producing a high DBCV index with identifying a reasonable number of clusters and noise points. With these goals, $n_{sample} = 2$, $n_{size} = 50$ and $\epsilon = 0.0$ are selected to produce $DBCV = 0.1745$, $n_{noise} = 30\%$ of the dataset, and $n_{clust} = 402$ clusters; this set of clusters is labeled $\mathcal{C}_{g,p}$ to reflect that the trajectories are grouped according to both geometry and phasing. This proportion of trajectories designated as noise is relatively high; reducing this percentage is an avenue of ongoing work.

Across the 402 clusters in $\mathcal{C}_{g,p}$, trajectories with perilunes evolution that exhibit similar geometry and phasing are grouped together. As an example, Figure 2 displays the perilune evolution of a subset of the trajectories in four clusters in the $e - \omega$ polar plot; each path is uniquely colored. The black curve highlights the perilune evolution of a single trajectory to facilitate comparison whereas red and blue markers locate the first and last perilunes, respectively. Within each subfigure, the evolution of the perilunes along each trajectory is geometrically similar with a similar phasing. However, the location and secular drift in the $e - \omega$ polar plot varies across the cluster. In addition, Figures 2a) and b) display two clusters capturing perilunes evolution with a similar geometry but distinct phasing. Alternatively, Figures 2c) and d) display two clusters that, when compared, contain geometrically distinct paths traced out by the perilunes in the $e - \omega$ polar plot. Accordingly, these four clusters demonstrate the capability of the clustering framework to group the generated lunar trajectories based on the geometry and phasing of their evolution of perilune.

Step 4: Extracting a cluster representative

To summarize each cluster, a cluster representative is extracted as the trajectory with the most bounded evolution of perilune in the pq-plane. This trajectory is identified as the sequence of perilunes that possesses the smallest cumulative distance, d_{seq}, between revolutions in the pq-plane.

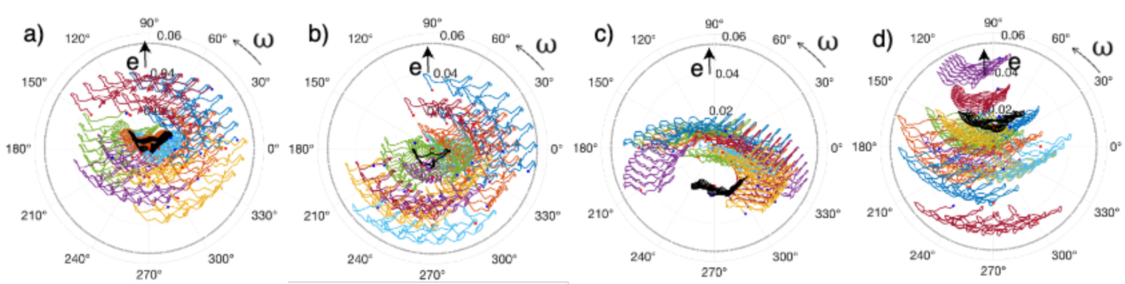

Figure 2. Perilune evolution of selected members of four clusters: sample member in black with red and blue points indicating the initial and final perilunes, respectively.

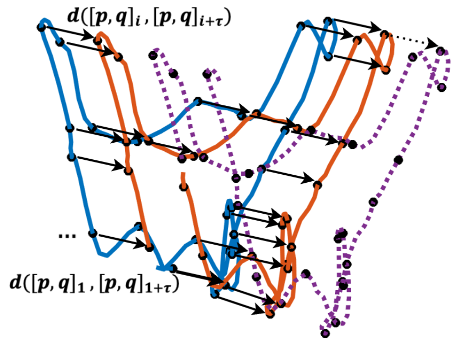

Figure 3. Calculating the distance between perilunes along neighboring revolutions in the pq-plane to identify a representative member of a cluster.

Recall that each revolution traced out by the perilunes in the pq-plane occurs over one lunar rotational period. Accordingly, a perilune path completes $w = P/P_l$ revolutions in the pq-plane where P is the integration time along the trajectory and P_l is the lunar rotational period. As a result, there are approximately $\tau = \lfloor m/w \rfloor$ perilunes sampled along each revolution. Using this approximation, the distance is calculated between the i-th sampled perilune that lies along the j-th revolution and the $i + \tau$-th sampled perilune in the pq-plane. This distance is displayed conceptually in Figure 3 as $d([p, q]_i, [p, q]_{i+\tau})$. Along the j-th revolution, the Euclidean distances between each sampled perilune and the associated perilunes along the $j + 1$-th revolution are averaged. These distances are computed between all subsequent revolutions and summed to produce the cumulative distance d_{seq}. The member of a cluster with the smallest value of d_{seq} is selected as the representative trajectory.

A representative trajectory is extracted from each cluster in $\mathcal{C}_{g,p}$ to support further analysis. Figure 4 displays an example of a cluster representative. In Figure 4a), the evolution of perilune is displayed in the Moon-fixed frame with the red and blue markers indicating the first and last perilunes, respectively. The evolution of perilune for this representative trajectory is also depicted in Figure 4b) in the $e - \omega$ polar plot. In this particular case, the evolution of perilune associated with this cluster representative exhibits only a small drift between subsequent revolutions both in the pq-plane and in the Moon-fixed frame. For additional examples, the black highlighted paths in Figure 2 are the representatives of those four clusters.

Step 5: Merging clusters with geometrically similar representatives

Members of multiple clusters in $\mathcal{C}_{g,p}$ may exhibit a geometrically similar evolution of perilune but are correctly separated due to distinct phasing of the initial and final perilunes. Accordingly, a second clustering step is used to merge clusters with a similar geometry, independent of phasing. This additional step is completed by using HDBSCAN to cluster only the representatives of each cluster from $\mathcal{C}_{g,p}$ with a new geometric feature vector and distance measure; the resulting set of clusters of representatives is labeled $\mathcal{C}_r$. For each group of representatives in $\mathcal{C}_r$, their associated clusters from $\mathcal{C}_{g,p}$ are merged. By applying this second clustering step to the cluster representatives, the increased computational expense associated with this new feature vector and distance measure does not become burdensome. The result of this second step is a set of clusters, each containing trajectories with a similar geometry regardless of the relative phasing of the initial and final perilunes.

A geometric feature vector is defined to describe the boundary of the path traced out by the

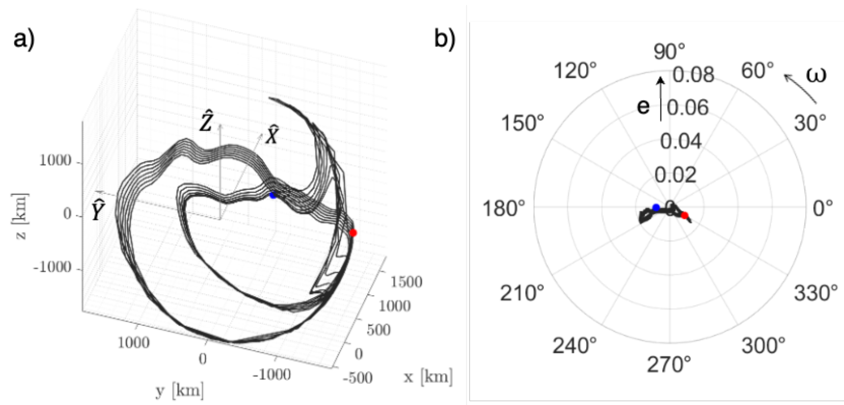

Figure 4. Perilune path associated with a cluster representative in the a) Moon-fixed frame and b) $e - \omega$ polar plot.

perilunes along each cluster representative in the pq-plane. This boundary is computed using shape-related functions in MATLAB.[41] First, the `alphaShape` function is applied to the ordered set of perilunes along the cluster representative to construct a convex polygon shape in the pq coordinates. Then, the pq coordinates of the perilunes that lie at the boundary of this polygon shape are extracted using the `boundaryFacets` function. Linear interpolation is used to extract a fixed number of pq coordinates that lie along each boundary to ensure that all cluster representatives are described by a boundary with the same resolution; the number of points is selected as the largest number of boundary perilunes calculated by the `boundaryFacets` function along the entire set of representatives. Then, the geometric feature vector $\bar{w}_i$ describing the i-th cluster representative is defined as

$$\bar{w}_i = [p_{B_1}, q_{B_1}, ..., p_{B_k}, q_{B_k}] \tag{8}$$

using the interpolated set of k boundary points B_j for $j = [1, k]$. Examples of the boundaries obtained from three sample perilune paths (black) in the pq-plane are displayed in Figure 5. In this figure, the left and center cluster representatives with blue boundaries possess a similar geometry and are, therefore, grouped together after clustering. The rightmost cluster representative with the red boundary, however, possesses a distinct geometry from the other two representatives.

To cluster the geometric feature vectors describing the representatives of $\mathcal{C}_{g,p}$ via HDBSCAN,

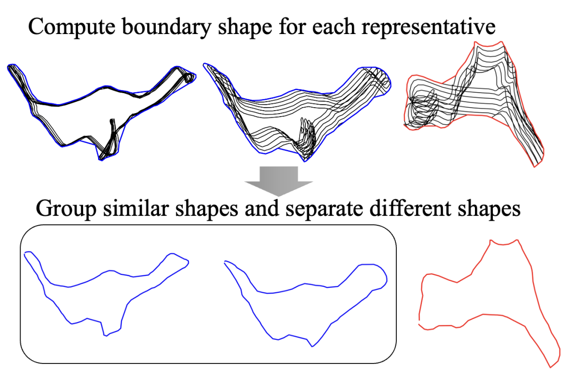

Figure 5. Computed boundaries of the paths traced out by perilunes along three trajectories in the $e - \omega$ plane.

multiple governing parameters must be selected. First, the values of the hyperparameters governing HDBSCAN are modified to $n_{sample} = 1$, $n_{size} = 2$, and $\epsilon = 0.08$ based on visual inspection of the clusters to accommodate the smaller dataset. Next, the modified Hausdorff distance d_{mhd} is used as a distance measure during this second clustering step to capture geometric differences in each path, independent of phasing. This distance measure is mathematically defined as:

$$d_{mhd}(\bar{v}_i, \bar{v}_j) = d_{mhd,f}(\bar{v}_i, \bar{v}_j) + d_{mhd,b}(\bar{v}_i, \bar{v}_j) \tag{9}$$

where

$$d_{mhd,f}(\bar{v}_i, \bar{v}_j) = \max_{i=1,..m} \big(\min_{j=1,..m} \|\bar{v}_i - \bar{v}_j\|_2 \big) \tag{10}$$

$$d_{mhd,b}(\bar{v}_i, \bar{v}_j) = \max_{j=1,..m} \big(\min_{i=1,..m} \|\bar{v}_i - \bar{v}_j\|_2 \big) \tag{11}$$

Due to the complexity of computing this distance measure, a higher computational time is required when compared to the Euclidean distance. However, the size of the reduced dataset of cluster representatives renders this computational time reasonable.

HDBSCAN is used to cluster the geometric feature vectors describing only the representatives of the clusters in $\mathcal{C}_{g,p}$. This second clustering step produces 41 clusters of representatives with similar geometry and 55 noise points. Representatives that exist in the same cluster in $\mathcal{C}_r$ indicate that their associated clusters from $\mathcal{C}_{g,p}$ should be merged. The cluster representatives labeled as noise points in $\mathcal{C}_r$, however, indicate that 55 of the original clusters from $\mathcal{C}_{g,p}$ should not be merged. Following the cluster merging process, there are 96 clusters of trajectories, labeled as the global clustering result $\mathcal{C}_g$ throughout the remainder of the paper to reflect that the trajectories are only grouped by geometry. Polar plots of the representative trajectories of these 96 clusters appear in the Appendix.

Visual inspection reveals that the merging process successfully combines trajectories with a similar geometry, regardless of phasing. An example of a merged cluster in $\mathcal{C}_g$ is displayed in Figure 6a), with each of 12 representatives from the original clusters in $\mathcal{C}_{g,p}$ uniquely colored. Each cluster representative from $\mathcal{C}_{g,p}$ exhibits a similar geometry in the $e - \omega$ plane. Figure 6b), also includes selected members of all 12 clusters from $\mathcal{C}_{g,p}$, displayed with the same color as the representative but a thin, transparent curve. The gray circle represents the value of eccentricity at impact with the Moon's surface when $a = 1838$ km. The region of the $e - \omega$ plane encompassed by members of this larger merged cluster indicates the region of existence of lunar trajectories with a similar geometric evolution in perilune but varying phasing, drift, and average eccentricities.

In addition to exhibiting a similar geometry in the $e - \omega$ polar plot, the 12 representatives that are plotted in Figure 6a) also exhibit a similar evolution of the remaining orbital elements. Figure 7 displays the range of values of the altitude, argument of perilune, eccentricity, inclination, and RAAN of perilunes along each cluster representative; each angle is calculated in the Moon-fixed frame. The orbital elements of each representative are colored using the same color scheme as Figure 6. The 12 representatives all begin with perilunes that exist at an inclination of $i = 75°$ in the Moon-fixed frame and exhibit only a small variation in this angle over time. Across all 12 representatives, the perilune altitude also varies by approximately 30 km over 180 days.

RESULTS

Using the presented technical approach, this section presents a broader analysis of the clustering-based summary of lunar trajectories generated in a high-fidelity model. First, several candidates for lunar frozen or quasi-frozen orbits are identified across the entire clustering result. Note, the phrase

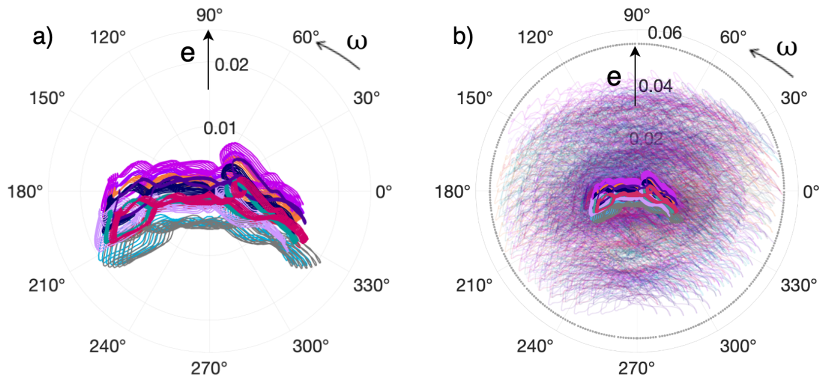

Figure 6. a) 12 representatives of clusters in $\mathcal{C}_{g,p}$ that are grouped based on geometry in the second clustering step. b) Selected members of the merged cluster in $\mathcal{C}_g$.

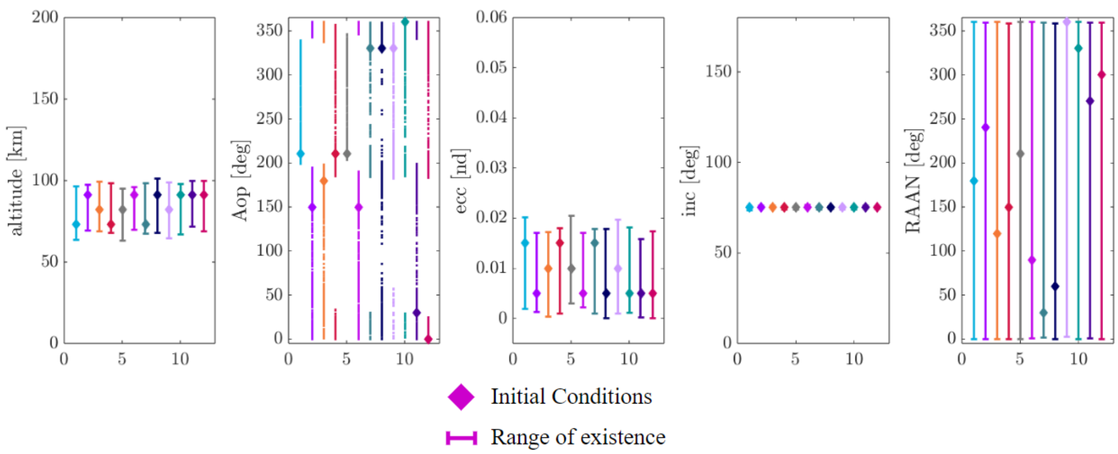

Figure 7. Initial orbital elements (diamond) with angles in the Moon-fixed frame associated with the 12 cluster representatives in Figure 6a) and their ranges of values during propagation.

'candidate for a frozen or quasi-frozen orbit' is used in this paper because 1) trajectories are only generated for 180 days and 2) the analysis is initially performed on the evolution of the eccentricity and argument of perilune; subsequent analysis requires examining the evolution of all orbital elements over longer time intervals. In addition, the clusters of trajectories with a geometrically similar evolution of perilune are used to identify local trends in the orbital elements that lead to changes in the orbit lifetime.

Identifying candidates for frozen orbits

By analyzing the final clustering result $\mathcal{C}_g$, trajectories with a tightly bounded evolution of perilune in the pq-plane and a lifetime of 6 months are analyzed as candidates for frozen orbits. As an example, consider the merged cluster of trajectories with a perilune evolution that is displayed in Figure 6. Figure 8 displays the perilunes along these 12 representative trajectories in Cartesian coordinates in the Moon-fixed frame using a different color scheme; each subfigure displays an alternative three-dimensional view for clarity. This figure reveals that these 12 representative tra-

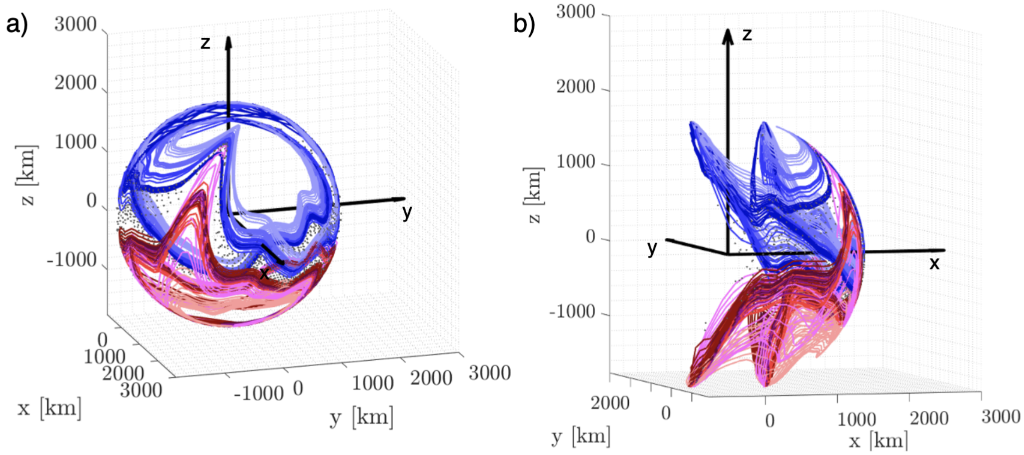

Figure 8. Uniquely-colored paths traced out by perilunes of 12 grouped cluster representatives in two different orientations in the Moon-fixed frame.

jectories exist in two groups. The perilune paths that are colored in shades of blue revolve around the $+Z$-axis of the Moon-fixed frame, aligned with the third lunar principal axis, twice every lunar rotational period. In the polar plot, the associated values of the argument of perilune in the Moon-fixed frame lie predominantly in the range $[0°, 180°]$. Similarly, the perilune paths that are colored in shades of red perform two revolutions around the $-Z$-axis of the Moon-fixed frame and possess arguments of perilune that are predominantly in the range $[180°, 360°]$. The perilunes along all 12 representative trajectories also predominantly pass over the $+X$ hemisphere of the Moon, corresponding to the first lunar principal axis and mean direction to the Earth.

The evolution of the perilune along grouped cluster representatives supports the visual identification of one or more candidates for low lunar frozen or quasi-frozen orbits. To understand this process, consider an analogy to a stable periodic orbit with nearby quasi-periodic orbits in the well-known planar circular restricted three-body problem. In this dynamical model, Poincaré maps are often used to examine the structure of the solution space. On a suitably constructed Poincaré map, stable periodic orbits appear as a fixed point that is surrounded by concentric closed curves corresponding to quasi-periodic orbits. When generating these Poincaré maps, a stable periodic orbit is rarely computed exactly. However, the presence of concentric curves and, therefore, a family of quasi-periodic orbits indicates the existence of the associated stable periodic orbit and supports locating its precise trajectory with the aid of differential corrections or other numerical methods.

Although the ephemeris model used in this paper is not autonomous and does not admit periodic orbits, the presented analogy is still useful. In Figures 6 and 8, the representative trajectories exhibit various levels of drift in the perilunes during each subsequent lunar rotational period. In this figure, the lower the drift, the darker the shade of blue or red of the path traced out by the perilunes of the associated trajectory. In this case, the perilune paths that are colored in the darkest shades of blue and red correspond to two trajectories with a perilune evolution that exhibits a low drift in the eccentricity over 180 days: one trajectory with a perilune predominantly over the northern hemisphere and the other over the southern hemisphere, supplying two suitable candidates for lunar frozen or quasi-frozen orbits. Future work will include numerically generating the trajectories for longer time intervals and/or using differential corrections to further reduce the drift in the eccentricity over time. Furthermore, future work will also include automatically assessing whether a cluster may contain multiple trajectories that are viable candidates for lunar frozen or quasi-frozen orbits and examining their evolution over various initial semi-major axes.

The manual identification of candidates for low lunar frozen and quasi-frozen orbits is repeated across all clusters in $\mathcal{C}_g$. For initial conditions that are constrained to possess a semi-major axis of 1838 km at January 1, 2025 00:00.000 UTC with the discretization scheme outlined in Step 1, a total of 15 candidates have been identified. These candidates possess various geometries in the evolution of perilune in both the pq-plane and the Moon-fixed frame. The initial conditions used to generate these 15 trajectories are displayed in the table contained within Figure 9, together with the variation in the perilune altitude during the 6-month propagation time. Of course, these initial conditions are not necessarily unique, but do supply insight into a combination of orbital elements that lead to each type of motion. Figure 10a)-d) also displays the paths traced out by the perilunes along these candidates in the $e-\omega$ polar plot. Each path is plotted with a unique color that matches the color in the first column of the table in Figure 9. For clarity, these 15 paths are separated across multiple plots based on their inclination.

Inclination	Eccentricity	AoP	RAAN	Variation in altitude
i = 0.001°	0.020	240°	299.990°	11.9 km
i = 20°	0.005	90°	270.0°	60.9 km
i = 25°	0.005	120°	270.0°	50.2 km
i = 50°	0.005	30°	330.0°	13.6 km
i = 70°	0.020	240°	180.0°	23.4 km
i = 75°	0.005	0°	300.0°	31.1 km
i = 80°	0.035	90°	270.0°	18.4 km
i = 85°	0.005	270°	270.0°	24.7 km
i = 95°	0.010	270°	150.0°	17.9 km
i = 100°	0.020	90°	90.0°	27.2 km
i = 105°	0.015	210°	330.0°	15.4 km
i = 130°	0.005	150°	120.0°	22.6 km
i = 135°	0.040	270°	330.0°	29.8 km
i = 160°	0.005	180°	30.0°	90.4 km
i = 179.999°	0.020	210°	210.005°	34.9 km

Figure 9. Initial orbital elements used to generate the 15 candidates for low lunar frozen orbits at $a = 1838$ km on January 1, 2025 00:00.000 UTC in a 100x100 gravity field. Colors in the first column match the color scheme in Figure 10

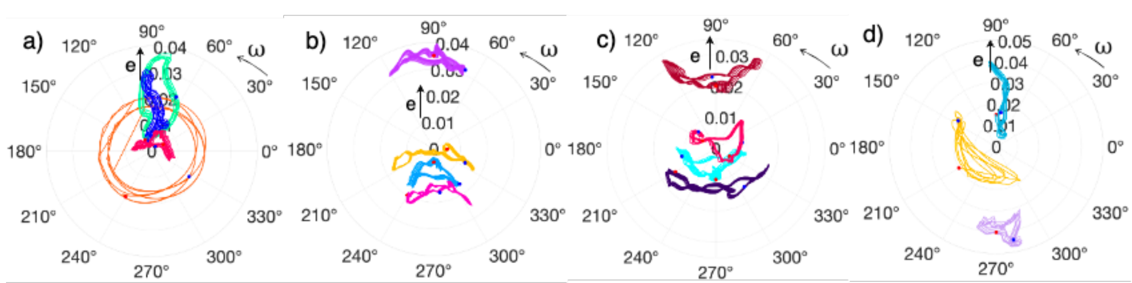

Figure 10. Evolution of perilune in the $e-\omega$ polar plot for the 15 candidates for low lunar frozen orbits at $a = 1838$ km at January 1, 2025 00:00.000 UTC in a 100x100 gravity field, grouped by initial inclination: a) from $i = 0.001°$ to $i = 50°$, b) from $i = 70°$ to $i = 85°$, c) from $i = 95°$ to $i = 130°$, and d) from $i = 135°$ to $i = 179.999°$. For each perilune, the red and blue dots indicate the initial and final states.

Some of the candidates for low lunar frozen orbits in Figure 10a)-d) have been identified by previous authors, offering verification of the results presented in this paper. For example, the candidates that exist at $75^\circ \leq i < 105^\circ$ match the frozen orbits presented in 2007 by Russell and Lara.[11] Lara also studied a frozen orbit at $i = 88^\circ$ with a similar perilune evolution to the candidate frozen orbit at $i = 85^\circ$.[42] Furthermore, Park and Junkins use the Lagrange planetary equations in a low-fidelity gravity model to derive combinations of the average eccentricity and inclination of frozen orbits at $a = 1838$ km when $\omega = 90^\circ$ or $\omega = 270^\circ$.[39] Some of the frozen orbits identified in this paper possess average values of i and ω that are similar to their findings; differences in eccentricity may be due to the use of single mean values and a lower-fidelity model. Lara, Ferrer, and De Saedeleer also identify low lunar frozen orbits with eccentricities between ~ 0 to 0.035 and initial arguments of perilune that place the initial perilune close to an axis of inertia, consistent with the properties of several candidates in Figure 10.[7] This result is also consistent with the conditions derived by Folta and Quinn using Lagrange's planetary equation, such that for $39.23^\circ < i < 140.77^\circ$, $\omega = 90^\circ$ or $\omega = 270^\circ$ corresponds to a value of eccentricity that drives $\dot{\omega}$ and $\dot{e}$ to zero.[5]

To further analyze the extracted candidates for lunar frozen orbits, their evolution of perilune is examined in the Moon-fixed frame. Specifically, Figure 11 displays a selection of the most bounded members of several clusters. Each subfigure displays a group of representatives that are clustered together in $\mathcal{C}_r$ during Step 5 of the presented framework. Trajectories with perilunes that predominantly exist in the northern hemisphere of the Moon are plotted in shades of blue whereas those with perilunes mostly in the southern hemisphere are plotted in shades of red. In the right inset of each subfigure, the path traced out by the most bounded trajectory in the $e - \omega$ polar plot appears along with the initial inclination labeled for reference.

The evolution of perilune along the candidates for frozen orbits is compared in the Moon-fixed frame. Figure 12 displays the perilune location along each trajectory in the Moon-fixed frame using unique colors; these colors do not match previous figures. Figure 12a) plots the perilune evolution for trajectories with a low inclination, as listed in the legend. Across this plot, the perilunes evolve with small variations in the latitude. Notably, trajectories with initial inclinations of $i = 1 \times 10^-3^\circ$ and $i = 179.999^\circ$ produce perilunes that are tightly bounded to a region that is slightly offset from the $-X$- and $+X$-axis, respectively. Figure 12b) displays the perilune evolution of trajectories with a higher inclination. In this case, the perilunes evolve over a larger range of latitudes, with some completing two revolutions in the Moon-fixed frame every lunar rotational period.

Figures 11 and 12 reveal near anti-symmetric properties in the candidates for frozen orbits as a function of inclination around $i = 90^\circ$. For instance, the trajectories with the most bounded evolution of perilune at $i = 20^\circ$ and $i = 160^\circ$ possess a similar geometry with perilunes occurring at near constant latitudes over the northern hemisphere of the Moon, except for one region where a ripple occurs. This ripple nearly anti-symmetrically occurs over the $+X$ and $-X$ hemispheres of the Moon, respectively. A similar observation holds for the trajectories with $i = 0.001^\circ$ and $i = 179.99^\circ$. The trajectories at high inclinations exhibit a slightly different geometry of the perilune evolution in the Moon-fixed frame: each path performs two revolutions near the $+/-Z$-axis. However, for $i = 85^\circ$, for example, this path spans the $+X$-hemisphere in the Moon-fixed frame whereas for $i = 95^\circ$, the perilunes exist predominantly over the $-X$-hemisphere. Aggregating these observations, the candidate lunar frozen orbits that are prograde and nonplanar produce perilunes that evolve most significantly over the $+X$-hemisphere whereas orbits that are retrograde and nonplanar possess perilunes that evolve most significantly in the $-X$ hemisphere. Although the X-axis is aligned with the mean direction to the Earth, a more extensive analysis of the dynamical

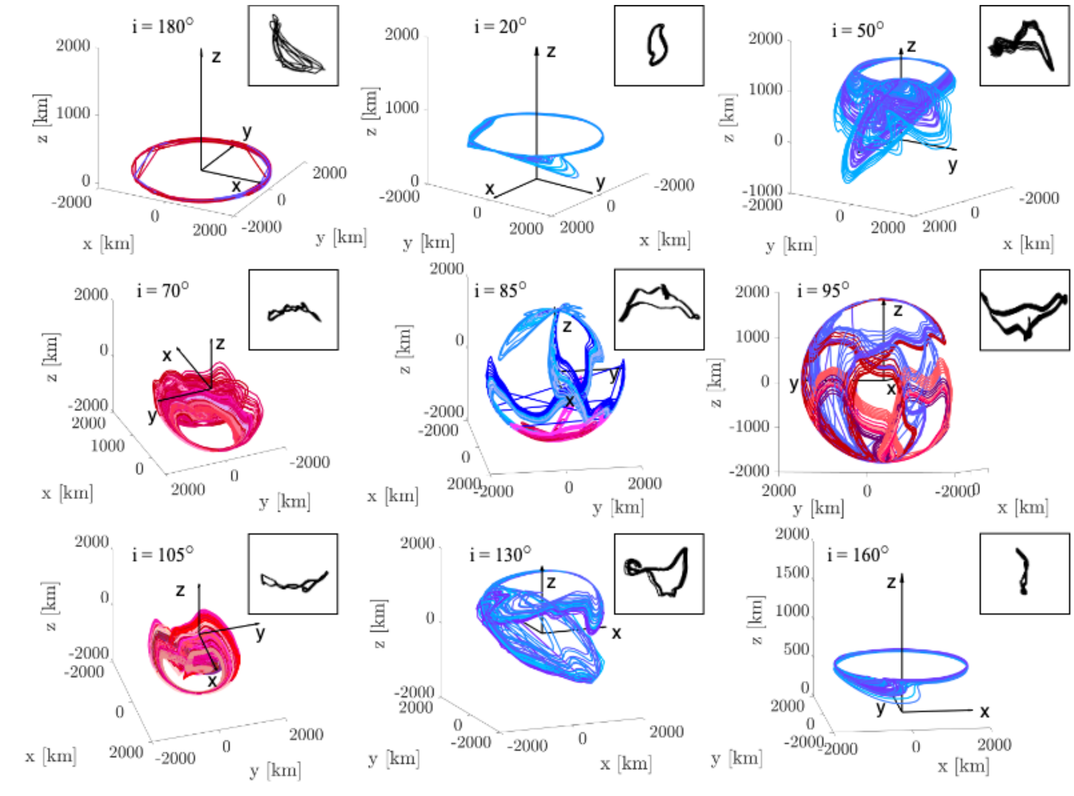

Figure 11. Perilune evolution in the Moon-fixed frame for selected representatives that are grouped together in $\mathcal{C}_r$ during Step 5 of the clustering-based framework. Perilunes that exist predominantly above the northern (or southern) hemisphere are colored blue (or red). Different orientations of the axes are used to best display the perilune geometries.

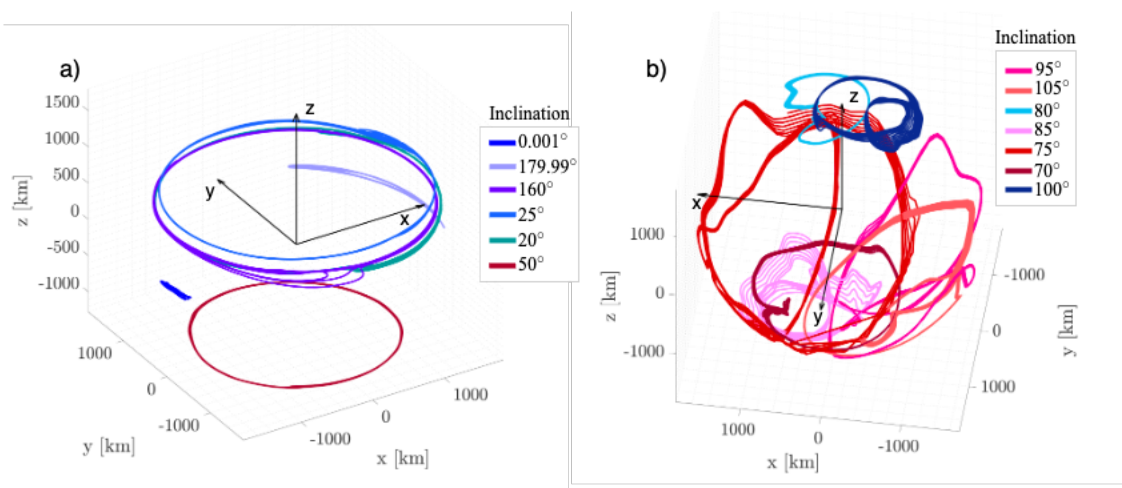

Figure 12. Evolution of perilune in the Moon-fixed frame for candidates for low lunar frozen orbits: a) low inclination trajectories and b) high inclination trajectories. These paths are colored in blue if the perilune lies predominantly over the northern hemisphere and red for the southern hemisphere.

contribution governing the characteristics of the perilune evolution in the Moon-fixed frame is an avenue of ongoing work.

Evolution of orbit lifetime in each cluster

Clusters of trajectories also support the identification of trends in the orbital elements that lead to changes in the orbit lifetime. Consider the 26 clusters that do not contain bounded motion and compare the evolution of trajectories across clusters at the same inclination when the eccentricity increases. The perilunes possess varying levels of drift and, as a result, orbit lifetimes. This drift tends to increase as the maximum eccentricity along the path increases. As an example, consider the time evolution of trajectories with an initial inclination of $i = 5°$ in Figure 13. For each trajectory, displayed on a single row, the following information is plotted from left to right: the evolution of perilune in the pq-plane; the variation in altitude over time, normalized by 180 days; the variation in inclination over time, normalized by 180 days; and the variation in eccentricity as a function of RAAN. At this inclination, the initial value of $e = 0.005$ produces a candidate for a frozen orbit, as displayed in the top row. However, as the initial eccentricity is increased to the values annotated in red in the right column of this figure, an increased drift occurs between the revolutions in the pq-plane over each lunar rotational period; simultaneously, the orbit lifetime decreases. At sufficiently high values of the eccentricity, the trajectory impacts the lunar surface in less than 1 lunar rotational period before completing a full revolution in the pq-plane.

Within $\mathcal{C}_g$, some clusters of trajectories with a lifetime of 180 days do not lead to frozen orbit candidates. Consider the representative trajectory of a cluster with $i = 90°$, plotted in Figure 14 a) in the $e - \omega$ polar plot along with the variation in its altitude, inclination, eccentricity, and RAAN.

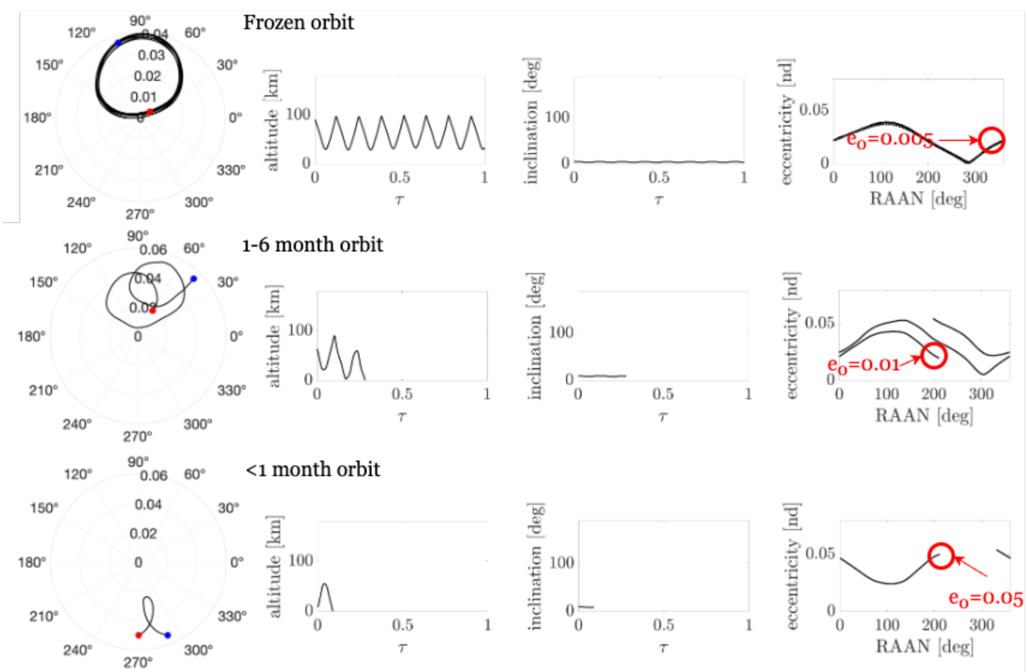

Figure 13. Comparing the evolution of the orbital elements for three orbits in a cluster at $i = 5°$: (top) frozen orbit, (center) orbit with 1-6 month lifetime and (bottom) orbit with < 1 month lifespan.

The perilune along this trajectory traces out a curve on average in the $e-\omega$ polar plot. This perilune evolution is similar to the evolution of paths that exist in the same cluster as a frozen orbit, e.g., in Figures 2 and 6. However, the perilunes along the trajectory in Figure 14a) and its associated cluster members intersect the lunar surface before completing a full revolution. Furthermore, the center of these curves traced out by the drifting perilune paths does not exist at an eccentricity that lies below the critical value corresponding to lunar impact at $a = 1838$ km. However, frozen orbits with a geometrically similar perilune evolution to this trajectory have been observed by Folta and Quinn to exist at $i = 90°$ with a higher-semi-major axis of $a = 1861$ km.[5]

The remaining 26 clusters within $\mathcal{C}_g$ that do not produce candidates for lunar frozen orbits include clusters of trajectories with a lifetime of less than 180 days. As an example, the evolution of perilune for members of two clusters is plotted in the pq-plane in Figure 14b) with $i = 120°$ and c) with $i = [160°, 180°]$. In Figure 14b), the perilunes of trajectories with a 1-6 month lifetime secularly drift towards the right in the pq-plane until impacting the lunar surface. Physically, this drift corresponds to the argument of perilune approaching $0°$ and, therefore, the perilune approaching a region around the mean direction to the Earth within the $\hat{X}\hat{Y}$ plane of the Moon-fixed frame. A similar secular drift in the perilune location within the pq-plane occurs in Figure 14c) for a group of trajectories with an orbit lifetime of less than 1 month.

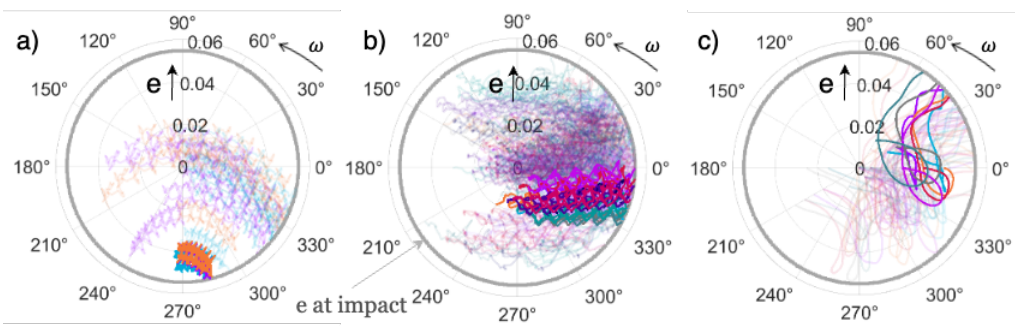

Figure 14. Evolution of perilune in the $e-\omega$ polar plot for two clusters of trajectories: a)with > 6 month lifetime but not bounded; b) with a 1-6 month orbit lifetime and c) with a <1-month orbit lifetime.

CONCLUSIONS

This paper uses clustering to summarize a wide variety of lunar trajectories and identify candidates for low-lunar frozen and quasi-frozen orbits. First, a large set of trajectories are numerically propagated in a high-fidelity lunar gravity model with the point mass gravity of the Earth and Sun. Then, the evolution of the eccentricity and argument of perilune at a subset of perilunes along these trajectories is described using a finite-dimensional feature vector that captures its shape. These feature vectors are input to a hierarchical and density-based clustering algorithm, producing groups of trajectories with a similar geometry and phasing the evolution of perilune. From each cluster, the most tightly bounded evolution of perilune produces a trajectory that serves as the cluster representative. These representatives are then described by their boundary to produce a geometric feature vector. The geometric feature vectors of only the cluster representatives are grouped again using a second clustering step. This grouping is used to merge clusters of trajectories with representatives that possess a similar geometry but distinct phasing. The result is a set of clusters of trajectories with a similar geometric evolution of perilune.

This paper applies the presented clustering-based framework to low lunar orbits generated from a wide variety of initial conditions with a semi-major axis of 1838 km at an initial epoch of January 1, 2025, 00:00.000 UTC. The resulting clusters of trajectories support the manual identification of 15 candidates for low lunar frozen orbits, each with a distinct geometry in their perilune evolution. Furthermore, the clusters support the identification of trends in the initial orbital elements that lead to changes in the orbit lifetime across a group of trajectories with a geometrically similar perilune evolution. Ongoing work focuses on extending this analysis to a larger set of trajectories across various semi-major axes, further examining the candidates for frozen orbits, and comparing the results across dynamical models of distinct fidelities.

ACKNOWLEDGMENTS

This work was completed at the University of Colorado Boulder with funding from NASA Grant 80NSSC22K1151. The first author is grateful for the Breakwell Student Paper Award and the Bahls Travel Award for supporting travel to this conference.

REFERENCES

[1] Y. Kozai, "Motion of a Lunar Orbiter," *Publications of the Astronomical Society of Japan*, Vol. 15, No. 8, 1963, p. 301.

[2] D. Folta, K. Galal, and D. Lozier, "Lunar Prospector Frozen Orbit Mission Design," *AIAA/AAS Astrodynamics Specialist Conference and Exhibit*, Boston, MA, August 1998.

[3] M. Beckman, "Mission Design for the Lunar Reconnaissance Orbiter," *29th Annual AAS Guidance and Control Conference*, Breckenridge, CO, February 2006.

[4] T. A. Ely, "Stable constellations of frozen elliptical inclined lunar orbits," *the Journal of the Astronautical Sciences*, Vol. 53, 2005, pp. 301–316.

[5] D. Folta and D. Quinn, "Lunar Frozen Orbits," *AIAA/AAS Astrodynamics Specialist Conference and Exhibit*, Keystone, CO, August 2006.

[6] A. Elipe and M. Lara, "Frozen Orbits About the Moon," *Journal of Guidance, Control, and Dynamics*, Vol. 26, No. 2, 2003, pp. 238–243.

[7] M. Lara, S. Ferrer, and B. De Saedeleer, "Lunar Analytical Theory for Polar Orbits in a 50-Degree Zonal Model Plus Third-Body Effect," *The Journal of the Astronautical Sciences*, Vol. 57, No. 3, 2009, pp. 561–577.

[8] J. F. San-Juan, A. Abad, A. Elipe, and E. Tresaco, "Analytical Model for Lunar Orbiter," *Advances in the Astronautical Sciences*, Vol. 130, January 2008, pp. 1669–1680.

[9] A. Abad, A. Elipe, and E. Tresaco, "Analytical Model to Find Frozen Orbits for a Lunar Orbiter," *Journal of Guidance, Control, and Dynamics*, Vol. 32, No. 3, 2009, pp. 888–898.

[10] S. Tzirti, K. Tsiganis, and H. Varvoglis, "Effect of 3rd-Degree Gravity Harmonics and Earth Perturbations on Lunar Artificial Satellite Orbits," *Celestial Mechanics and Dynamical Astronomy*, Vol. 108, No. 4, 2010, pp. 389–404.

[11] R. P. Russell and M. Lara, "Long-Lifetime Lunar Repeat Ground Track Orbits," *Journal of Guidance, Control, and Dynamics*, Vol. 30, No. 4, 2007, pp. 982–993.

[12] J. Han, J. Pei, and M. Kamber, *Data Mining: Concepts and Techniques*. The Morgan Kaufmann Series in Data Management Systems, Morgan Kaufmann, second edition ed., March 2006.

[13] J. L. Bruse, M. A. Zuluaga, A. Khushnood, K. McLeod, H. N. Ntsinjana, T.-Y. Hsia, M. Sermesant, X. Pennec, A. M. Taylor, and S. Schievano, "Detecting Clinically Meaningful Shape Clusters in Medical Image Data: Metrics Analysis for Hierarchical Clustering Applied to Healthy and Pathological Aortic Arches," *IEEE Transactions on Biomedical Engineering*, Vol. 64, No. 10, 2017, pp. 2373–2383.

[14] C.-B. Tohill, S. Bamford, and C. Conselice, "Exploring the Morphologies of High Redshift Galaxies with Machine Learning," *Memorie della Società Astronomica Italiana*, Vol. 75, February 2023, pp. 282–286.

[15] B. Villac, R. Anderson, and A. Pini, "Computer Aided Ballistic Orbit Classification Around Small Bodies," *Journal of Astronautical Sciences*, Vol. 63, No. 3, 2016, pp. 175–205.

[16] A. Hadjighasem, D. Karrasch, H. Teramoto, and G. Haller, "Spectral-Clustering Approach to Lagrangian Vortex Detection," *Physical Review E*, Vol. 93, No. 6, 2016.

[17] N. Nakhjiri and B. F. Villac, "Automated Stable Region Generation, Detection, and Representation for Applications to Mission Design," *Celestial Mechanics and Dynamical Astronomy*, Vol. 123, No. 1, 2015, pp. 63–83.

[18] T. Smith and N. Bosanac, "Constructing Motion Primitive Sets to Summarize Periodic Orbit Families and Hyperbolic Invariant Manifolds in a Multi-Body Systems," *Celestial Mechanics and Dynamical Astronomy*, Vol. 134, No. 7, 2022.

[19] N. Bosanac, "Data-Mining Approach to Poincaré Maps in Multi-Body Trajectory Design," *Journal of Guidance, Control, and Dynamics*, Vol. 43, No. 6, 2020, pp. 1190–1200.

[20] S. Bonasera and N. Bosanac, "Applying data mining techniques to higher-dimensional Poincaré maps in the circular restricted three-body problem," *Celestial Mechanics and Dynamical Astronomy*, Vol. 133, Dec. 2021, p. 51.

[21] R. Campello, D. Moulavi, and J. Sander, "Density-Based Clustering Based on Hierarchical Density Estimates," *Advances in Knowledge Discovery and Data Mining* (J. Pei, V. Tseng, L. Cao, H. Motoda, and G. Xu, eds.), Springer Berlin, Heidelberg, 2013, p. 160–172.

[22] D. Folta, N. Bosanac, I. Elliott, L. Mann, R. Mesarch, and J. Rosales, "Astrodynamics Convention and Modeling Reference for Lunar, Cislunar, and Libration Point Orbits," tech. rep., 2022.

[23] NASA Goddard Space Flight Center, "A Standardized Lunar Coordinate System for the Lunar Reconnaissance Orbiter and Lunar Datasets ," October 2008.

[24] C. H. Acton, "Ancillary data services of NASA's Navigation and Ancillary Information Facility," *Planetary and Space Science*, Vol. 44, No. 1, 1996, pp. 65–70. Planetary data system.

[25] C. Acton, N. Bachman, B. Semenov, and E. Wright, "A look towards the future in the handling of space science mission geometry," *Planetary and Space Science*, Vol. 150, 2018, pp. 9–12. Enabling Open and Interoperable Access to Planetary Science and Heliophysics Databases and Tools.

[26] W. M. Folkner, J. G. Williams, and D. H. Boggs, "The Planetary and Lunar Ephemeris DE 421," *Interplanetary Network Progress Report*, Vol. 42-178, Aug. 2009, pp. 1–34.

[27] D. A. Vallado, *Fundamentals of Astrodynamics and Applications*. Microcosm Press and Springer, 4th ed., 2013.

[28] F. G. Lemoine, S. Goossens, T. J. Sabaka, J. B. Nicholas, E. Mazarico, D. D. Rowlands, B. D. Loomis, D. S. Chinn, G. A. Neumann, D. E. Smith, and M. T. Zuber, "GRGM900C: A degree 900 lunar gravity model from GRAIL primary and extended mission data," *Geophysical Research Letters*, Vol. 41, No. 10, 2014, pp. 3382–3389.

[29] A. Konopliv, S. Asmar, E. Carranza, W. Sjogren, and D. Yuan, "Recent gravity models as a result of the Lunar Prospector mission," *Icarus*, Vol. 150, No. 1, 2001, pp. 1–18.

[30] J. Han, J. Pei, and M. Kamber, "Data mining: concepts and techniques," 2011.

[31] R. J. Campello, D. Moulavi, and J. Sander, "Hierarchical density estimates for data clustering, visualization, and outlier detection," *ACM Transactions on Knowledge Discovery from Data (TKDD)*, Vol. 10, No. 1, 2015, p. 5.

[32] S. Gare, S. Chel, P. D. Pantula, A. Saxena, K. Mitra, R. Sarkar, and L. Giri, "Analytics Pipeline for Visualization of Single Cell RNA Sequencing Data from Brochoaveolar Fluid in COVID-19 Patients: Assessment of Neuro Fuzzy-C-Means and HDBSCAN," *2022 44th Annual International Conference of the IEEE Engineering in Medicine Biology Society (EMBC)*, 2022, pp. 1634–1637.

[33] A. Leonard, S. Wheeler, and M. McCulloch, "Power to the people: Applying citizen science and computer vision to home mapping for rural energy access," *International Journal of Applied Earth Observation and Geoinformation*, Vol. 108, 2022, p. 102748.

[34] C. Malzer and M. Baum, "A hybrid approach to hierarchical density-based cluster selection," *2020 IEEE international conference on multisensor fusion and integration for intelligent systems (MFI)*, IEEE, 2020, pp. 223–228.

[35] L. McInnes, J. Healy, and S. Astels, "hdbscan: Hierarchical density based clustering," *Journal of Open Source Software*, Vol. 2, No. 11, 2017, p. 205.

[36] D. Moulavi, P. A. Jaskowiak, R. J. G. B. Campello, A. Zimek, and J. Sander, "Density-Based Clustering Validation," *Proceedings of the 2014 SIAM International Conference on Data Mining*, Society for Industrial and Applied Mathematics, pp. 839–847.

[37] D. Brouwer, "Solution of the problem of artificial satellite theory without drag," tech. rep., Yale University New Haven CT, United States, 1959.

[38] M. Rosengren, "Improved technique for passive eccentricity control," *Orbital Mechanics and Mission Design*, Jan. 1989, pp. 49–58.

[39] S.-Y. Park and J. Junkins, "Orbital mission analysis for a lunar mapping satellite," *Astrodynamics Conference*, 1994, p. 3717.

[40] K. R. Lang, *Astrophysical data: Planets and stars*. Springer Science & Business Media, 2012.

[41] MATLAB, *version R2014b*. Natick, Massachusetts: The MathWorks Inc., 2013-2015.

[42] M. Lara, "Design of long-lifetime lunar orbits: A hybrid approach," *Acta Astronautica*, Vol. 69, No. 3, 2011, pp. 186–199.

APPENDIX

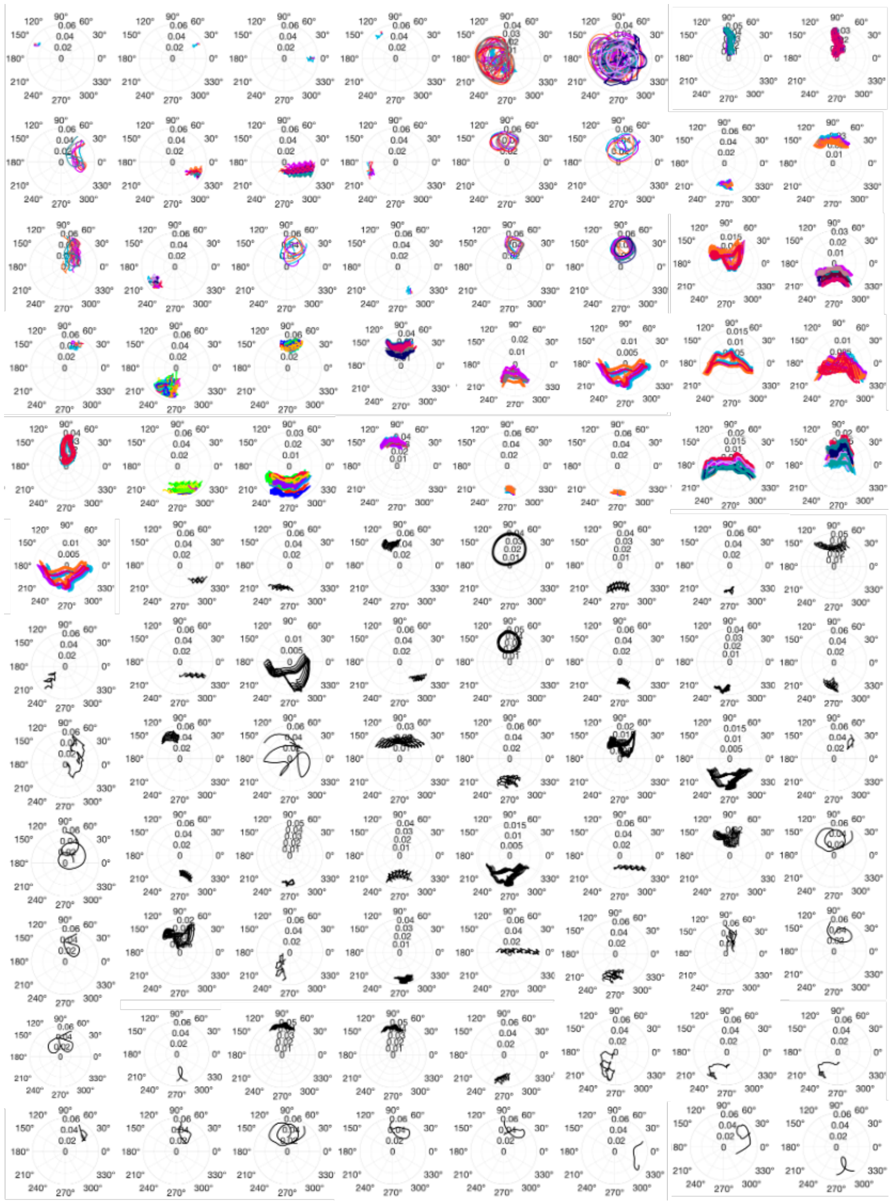

Figure 15. Perilune evolution in the $e - \omega$ polar plot for representative members of clusters in $\mathcal{C}_g$: black representatives are isolated clusters that were not merged in Step 5 whereas colored representatives correspond to clusters that were merged.